SCALE ADAPTIVE FLOW SIMULATION IN A GENERIC MIXING MANIFOLD

W. Hassler
B. Wiesler
A. Tramposch

FH JOANNEUM Gesellschaft mbH
Alte Poststraße 149
8020 Graz, Austria

Abstract

The purpose of the mixing manifold in passenger aircraft is to mix recirculating hot air coming from the cabin with preconditioned cold air which is diverted from the engines. In the present paper computations of the unsteady flow field as well as investigations of scalar mixing in a generic mixing manifold are described. The turbulence models utilized for the simulations are the scale resolving SAS-SST turbulence model on the one hand, and the SSG-Reynolds Stress Transport model – a "conventional" URANS model – on the other hand.

NOMENCLATURE

M	Mass fraction, $kg \cdot kg^{-1}$
Q	Q-invariant of the velocity-gradient tensor, $Q = \frac{1}{4}\left(\omega_i \omega_i - 2S_{ij}S_{ij}\right)$, s^{-2}
S_{ij}	Strain tensor, s^{-1}
u_i	i-th Cartesian velocity component, $m \cdot s^{-1}$
UDS1	First order upwind differencing scheme
UDS2	Second order upwind differencing scheme
x_i	i-th Cartesian coordinate, m
ω_i	i-th Cartesian component of the vorticity vector, s^{-1}

1. INTRODUCTION

A pivotal structural component of the air conditioning system in passenger aircraft is the mixing unit (MU). Its purpose is to mix recirculating hot air coming from the cabin and the cockpit (recirc air) with bleed air which is diverted from the engines and preconditioned by packs (pack air). After the mixing process has taken place within the MU, the air gets redistributed throughout the aircraft.

In order to optimize the performance of the MU it is important to understand the mixing process in greatest possible detail. The main emphasis of the research described in this article lies on the investigation and pre-selection of appropriate turbulence models for CFD-simulations of the flow field and thermal (equivalently, scalar) mixing in the MU. The current investigations were performed in the simplified mixer geometry depicted in Figure 2.1 in order to understand the main characteristics and basic structure of the flow field. In the course of ongoing investigations the current results provide a good basis for simulations in more complex geometries. As part of a running research project carried out at FH JOANNEUM, refined mixer simulations are performed and then validated by means of experimental data obtained from LDA-measurements and scalar mixing experiments. Thereby the simulations and experiments will be carried out with realistic prototypes of aeronautical mixing manifolds.

After the current research has begun it became apparent quickly that a broad range of flow regimes is present in the MU. For instance, the selection of appropriate simulation methods and turbulence models must take into consideration flow phenomena such as swirling flow within the cylindrical section of the MU, colliding jets entering the MU through the inlet ducts, vortex breakdown in the MU and – last but not least – thermal and scalar mixing in the MU.

Several papers have so far been written on mixing manifolds. In an early paper published in 1985 by Eggebrecht et al. [4] this involved component – as it can be seen nowadays on Airbus and Boeing aircraft – is described and investigated. In this modern design the cylindrical section of the MU and the different inlets are arranged in such a way that the flows are subjected to a sudden expansion, which is the first step to flow homogenization. Further, the inlet ducts are organized in such a way that swirl flow is created within the MU. This potently improves the mixing.

In 2007 Bourlart and Landais [3] investigated vortex

breakdown in the cylindrical section of the MU and aero-acoustic noise production interlinked therewith. The two authors performed flow simulations as well as acoustic measurements for several arrangements and configurations of inlets, boundary conditions and types of vortex generators. They came to the conclusion that for some configurations vortex breakdown is present and for other – fairly similar – configurations it is not. In other words, the presence of vortex breakdown (which – according to findings of the authors – positively affects the mixing performance of the MU) depends on the detailed configuration that is considered. Vortex breakdown in the context of the present investigations is discussed in more detail at the end of Section 2.

The mass ratio of pack air and recirc air passing through a MU is approximately 60% pack air : 40% recirc air. The pack air temperature may be below 0°C, whereas the recirculation air temperature lies – under normal operating conditions – roughly in the range 15°C – 35°C*. Due to the (normally) low temperature and the presence of remnant humidity in the pack air, this air stream may contain frost particles. Further, if the humidity of the recirculation air exceeds a certain threshold, then additional frost may form when the hot recirc air comes in contact with the cold pack air. Subsequently, the ice particles that are formed may clog parts of the MU and impair or even disrupt its operability. However, if pack air and recirc air could be mixed immediately and perfectly, then the temperature of the air mix would be above 0°C, and no frost would form. To reduce or even prevent frost formation it is thus important that the mixing of pack air and recirc air takes place as quickly and as thoroughly as possible.

The flow simulations described in this paper were performed in ANSYS CFX 11.0, and the computational grids were created with the aid of ANSYS ICEM 11.0. Parallel computations included up to 20 Intel Xeon X5355 CPUs at a clock rate of 3 GHz. The amount of RAM-storage available throughout the simulations was 4 GB per CPU.

2. FLOW SIMULATIONS IN A SYMMETRIC MIXING MANIFOLD

In the current section simulations with F. Menter's Scale Adaptive Shear Stress Transport model (SAS-SST model) as well as with the SSG Reynolds Stress Transport model (SSG-RST model) – a "conventional" URANS-model – are described. For details regarding the SST and SAS-SST models the reader is referred to [7, 8, 9, 10, 11]. A major motivation for using an RST-model in the current investigations was the successful utilization of this type of turbulence model for mixer simulations in [3]. On the other hand, an important reason for choosing the SAS-model was its promising application to simulations of thermal mixing in a T-pipe. Such simulations were performed recently by the authors and subsequently validated by means of experimental data and simulation results described in [6] and [12].

The current simulations were carried out in the simplified and highly symmetric mixer geometry depicted in Figure 2.1. An important reason for choosing this geometric configuration was to study symmetry properties of the flow field. It turned out that the time-averaged flow field fails to reflect the full symmetry of the geometry and boundary conditions. More details on this issue can be found in the "Remarks and conclusions" part at the end of the section.

The origin of the Cartesian coordinate system used to describe the geometry depicted in Figure 2.1 is located at the center of the circular bottom of the large central cylinder. The diameter of the large central cylinder is 0.78 m and its height is 2.18 m. The length of the inlet pipes is 0.9 m and their diameter is 0.39 m. The length of the outlet pipes is 3 m with diameter 0.5 m. The center lines of the inlet pipes have z-coordinate 0.27 m, and the centerlines of the outlet pipes have z-coordinate 1.78 m. The geometry as well as the computational grid are mirror-symmetric with respect to both the xz-plane and the yz-plane.

In the present simulations also turbulent mixing of passive scalars was considered. More precisely, the mass fractions

$$M_1 = \frac{A_1}{A_1 + A_2} \quad \text{and} \quad M_2 = \frac{A_2}{A_1 + A_2}$$

were studied, where the quantities A_1 resp. A_2 denote the total concentrations (with physical unit $kg \cdot kg^{-1}$) of air coming from Inlet 1 resp. Inlet 2.

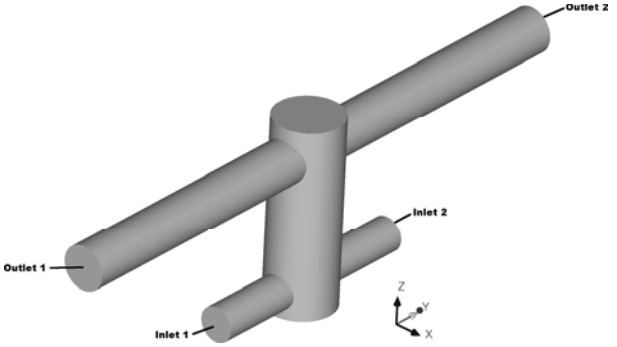

Figure 2.1: Symmetric mixer geometry for the simulations with the SAS-SST and SSG-RST turbulence models

In Table 2.2 the settings that are common for the current SAS-SST and SSG-RST simulations are listed. The advection scheme termed "High Resolution" in Table 2.2 is a dynamic blend of the UDS1 scheme (upwind differencing scheme of first order – cf. for instance [2, 5]) and the UDS2 scheme (upwind differencing scheme of second order – see for instance [2, 5]). The determination of the blend factor is based on boundedness principles described in [2]. The High Resolution scheme is the standard advection scheme for RANS and URANS simulations in CFX 11.0. For a more detailed discussion of this scheme the reader is referred to the CFX 11.0 manual [1].

* In certain exceptional cases, e.g. if the interior of the aircraft is at low temperature and must be heated, the recirc air temperature may be below 0°C. In these cases the pack air temperature must be raised up to 70°C in order to arrive at an appropriate temperature level of the air mix.

Table 2.2: Common parameters for the SAS-SST and SSG-RST simulations

Grid type	Tetrahedral with prism layer
Medium	Air Ideal Gas at 15°C
Mass flow rate	2.4 $kg \cdot s^{-1}$ for each inlet
Velocity profile at inlets	Constant and normal to boundary
Turbulence intensity at inlet boundaries	5%
Static pressure at outlet boundaries	Constantly 1 atm over whole boundary
Time discretization scheme	Second order Euler implicit
Advection scheme (mass, momentum, turbulence equations, mass fraction)	High Resolution
Time interval for temporal averaging of the physical parameters	5 s
Number of inner loop iterations during each time step iteration	3

In Table 2.3 the individual settings of the four simulations that will be described below are listed. The same grids were used for Configurations 1 and 3. Similarly, identical grids were used for Configurations 2 and 4. Both grids are mirror-symmetric with respect to both the *xz*-plane and the *yz*-plane. Figures 2.4 – 2.7 illustrate the fine mesh in several cross sections. The typical cell size of the fine grid near the centerline of the main cylinder in the lower and upper density regions (z ~ 0.25 m and z ~ 1.75 m) is approximately 15 mm. The cell size near the centerline at z ~ 1 m is approximately 30 mm for the fine grid. Due to the creation process using the octree method, the grids are fairly regular at locations which are a certain distance off the wall. They become more irregular in the neighborhood of walls (cf. Figures 2.4 – 2.6). This irregularity is also present in the vicinity of the two symmetry planes since first one quarter of the geometry was meshed, and then the grid was reflected at the *xz*- and the *yz*-plane.

The wall treatment setting “Automatic” in Table 2.3 means an automatic switching from the use of wall-functions to a low Reynolds formulation if the (local) grid resolution allows a full resolution of the boundary layer. More details on this wall treatment model can be found in the CFX 11.0 manual [1]. It is noted that, for the current computations, the choice of automatic wall treatment essentially means that wall-functions were used. The reason is that – for most parts of the domain – the near-wall grid resolution is not sufficient to fully resolve the boundary layer (cf. the y+-values listed in Table 2.8). The wall treatment setting “Scalable” means that scalable wall-functions were used – see [1] for details.

Table 2.3: Individual settings for the SAS-SST and SSG-RST simulations

	Config. 1	**Config. 2**	**Config. 3**	**Config. 4**
Turbulence model	SAS-SST	SAS-SST	SSG-RST	SSG-RST
Wall treatment	Automatic	Automatic	Scalable	Scalable
Number of grid nodes	$5 \cdot 10^5$	$9.4 \cdot 10^5$	$5 \cdot 10^5$	$9.4 \cdot 10^5$
Number of volume elements	$2 \cdot 10^6$	$3.7 \cdot 10^6$	$2 \cdot 10^6$	$3.7 \cdot 10^6$
Time step size, s	$2 \cdot 10^{-3}$	10^{-3}	$2 \cdot 10^{-3}$	10^{-3}
Initial values obtained from	a successive reduction of the time step size	Config. 1 with grid interpolation	a computation using UDS1	Config. 3 with grid interpolation

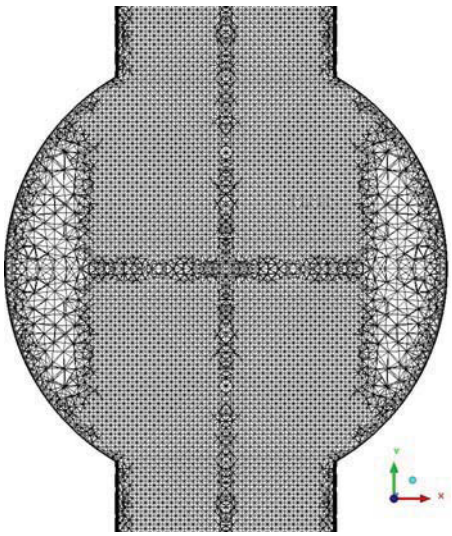

Figure 2.4: Section of the fine grid by the plane z = 0.25 m

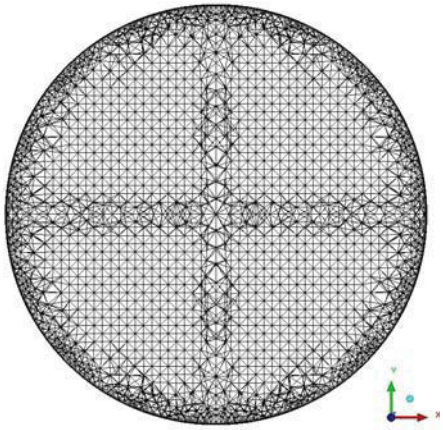

Figure 2.5: Section of the fine grid by the plane z = 1 m

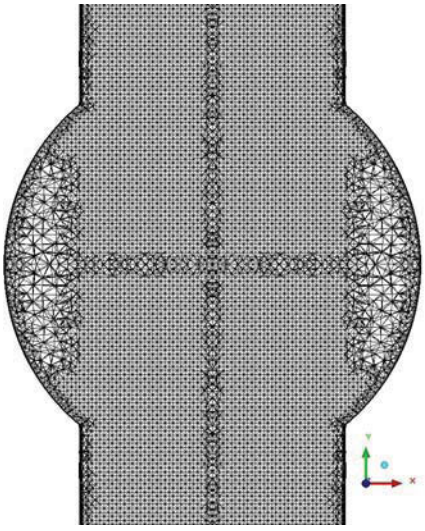

Figure 2.6: Section of the fine grid by the plane z = 1.75 m

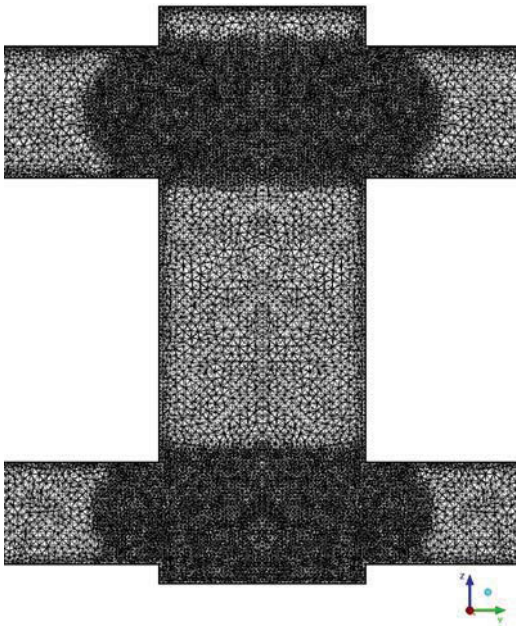

Figure 2.7: Section of the fine grid by the plane x = 0 m

In Table 2.8 several target parameters obtained from the simulation results are listed. All these target quantities are time-averaged and, as specified in Table 2.8, also spatially averaged over certain locations.

Table 2.8: Comparison of time-averaged target parameters

	Config. 1	Config. 2	Config. 3	Config. 4
Average y+ value at the cylinder wall	15	15	15	16
RMS CFL number	2.9	1.8	2.9	1.8
RMS local mass imbalance	10^{-4}	$8{\cdot}10^{-5}$	10^{-4}	$5{\cdot}10^{-5}$
RMS local *x*-mom. imbalance	$2{\cdot}10^{-4}$	$8{\cdot}10^{-5}$	$6{\cdot}10^{-4}$	$9{\cdot}10^{-5}$
RMS local *y*-mom. imbalance	$2{\cdot}10^{-4}$	$9{\cdot}10^{-5}$	$4{\cdot}10^{-4}$	$6{\cdot}10^{-4}$
RMS local *z*-mom. imbalance	$2{\cdot}10^{-4}$	$9{\cdot}10^{-5}$	$6{\cdot}10^{-4}$	$8{\cdot}10^{-4}$
Flow field orientation	anticlockwise	anticlockwise	anticlockwise	anticlockwise
Static pressure loss, averaged over Inlet 1, hPa	3.9	3.6	3.8	3.9
Static pressure loss, averaged over Inlet 2, hPa	3.9	3.7	3.8	3.9
Mass flow rate at Outlet 1, kg·s^{-1}	2.43	2.38	2.40	2.39
Mass flow rate at Outlet 2, kg·s^{-1}	2.37	2.42	2.40	2.41
Mass fraction M_1, averaged over Outlet 1	0.56	0.55	0.55	0.57
Mass fraction M_1, averaged over Outlet 2	0.43	0.44	0.45	0.43
CPU-time in days	53.6	96.7	67.0	210.2

In Figure 2.9 a streamline plot of the time-averaged velocity field is shown. The colors do not have a direct physical meaning; the different coloring of the streamlines starting from Inlet 1 and Inlet 2 was chosen for a better visualization of the vortical flow field in the main cylinder of the MU. Figure 2.10 shows a couple of streamlines of the time-averaged flow field for Configuration 2. In Figures 2.11 through 2.13 vector plots of the time-averaged flow field for several sections through the flow geometry are depicted. Figure 2.14 shows an isosurface plot of the *Q*-invariant for the instantaneous flow field of Configuration 2. The coloring visualizes the mass fraction M_1 in the range 0.25 – 0.75. Figure 2.15 shows the time-dependent mass fraction M_1 averaged over Outlets 1 and 2. Figures 2.16 – 2.19 show various additional aspects of the simulation results. These issues will be discussed in the part “Remarks and Conclusions” at the end of the section.

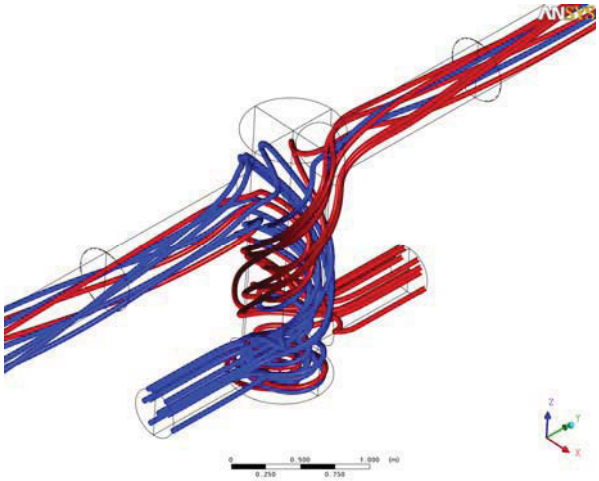

Figure 2.9: Streamlines with non-physical coloring for a better visualization of the core vortex in the main cylinder

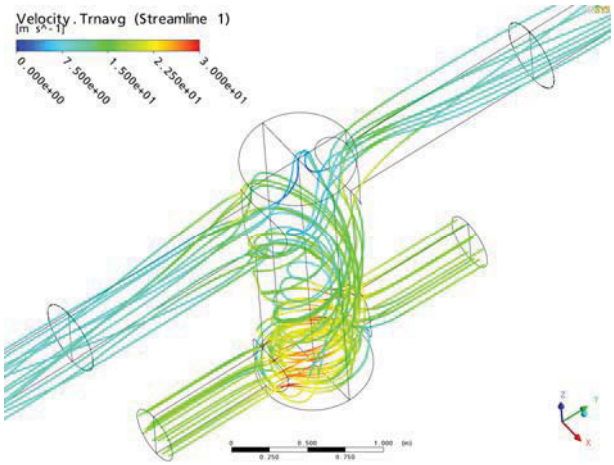

Figure 2.10: Streamline plot based on the time-averaged velocity field, Config. 2.

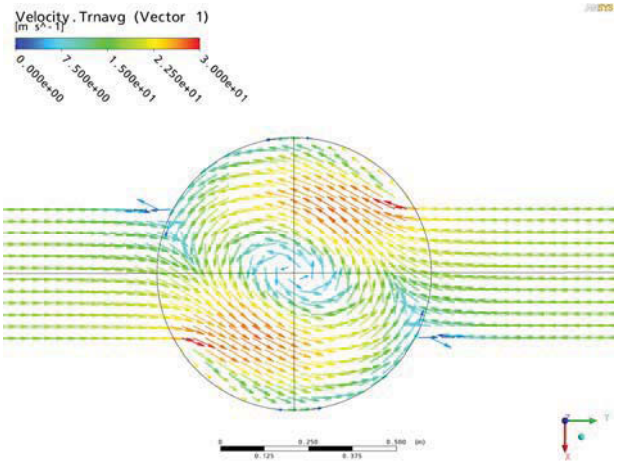

Figure 2.11: Vector plot of the time-averaged velocity field in the plane z = 0.25 m, Config. 2

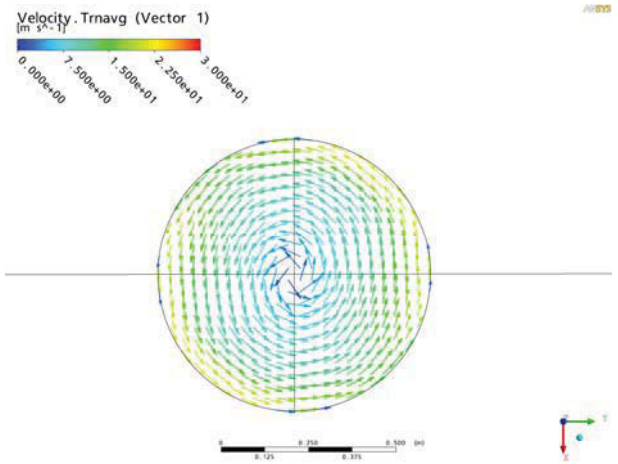

Figure 2.12: Vector plot of the time-averaged velocity field in the plane z = 1 m, Config. 2

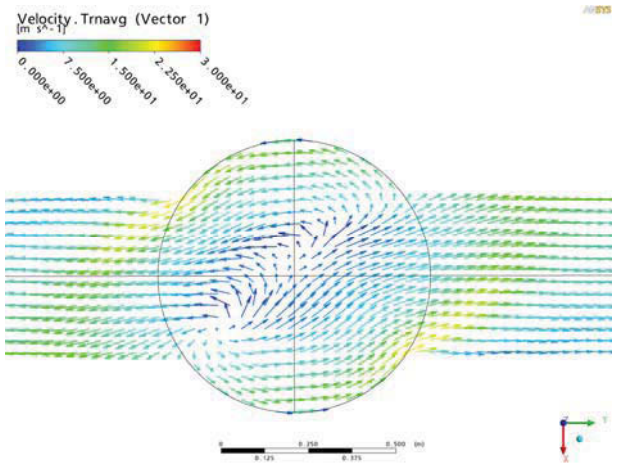

Figure 2.13: Vector plot of the time-averaged velocity field in the plane z = 1.75 m, Config. 2

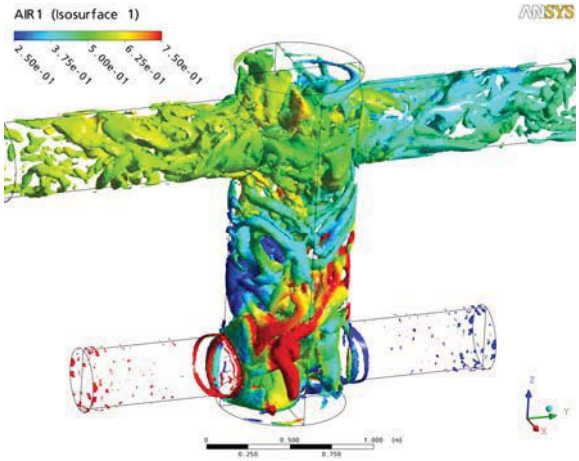

Figure 2.14: Isosurface at Q = 5000 in order to visualize the turbulent structures in the MU, colored by the mass-fraction variable M_1 in the range 25% – 75%, Config. 2

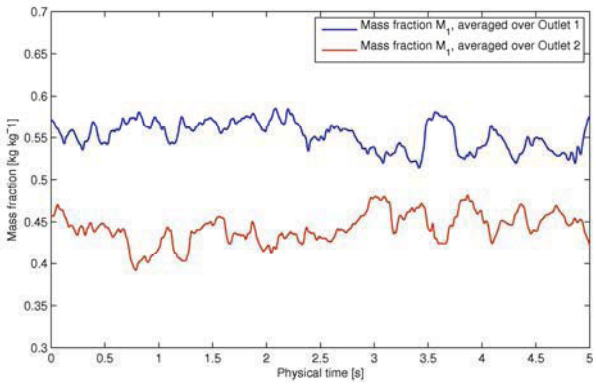

Figure 2.15: Time-dependent mass fraction M_1, averaged over Outlets 1 and 2, Config. 2

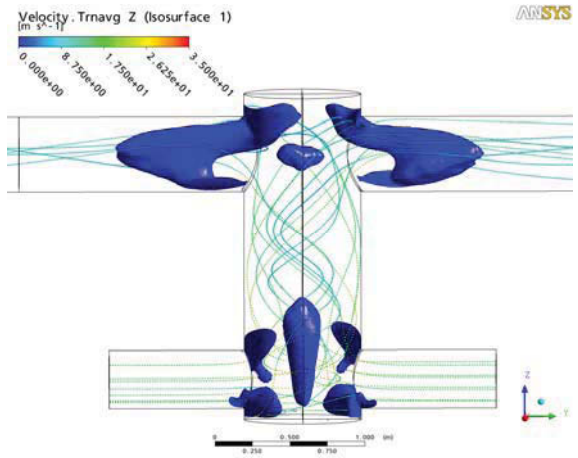

Figure 2.16: Isosurface $\langle u_z \rangle$ = –2 m·s^{-1} of the time-averaged velocity field, Config. 2

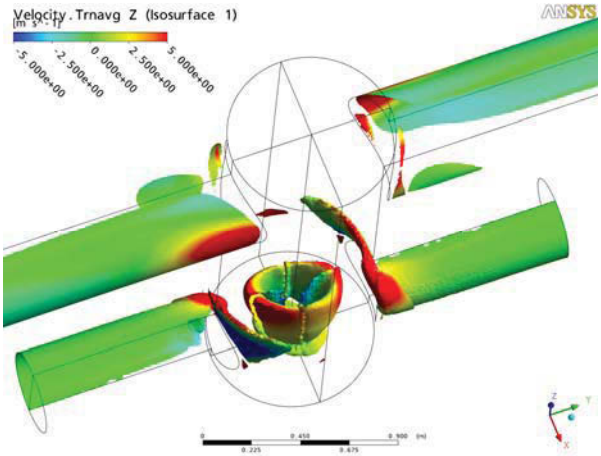

Figure 2.17: Isosurface plot of $\langle\omega_z\rangle$ = 250 s^{-1}, colored by $\langle u_z\rangle$, Config. 4

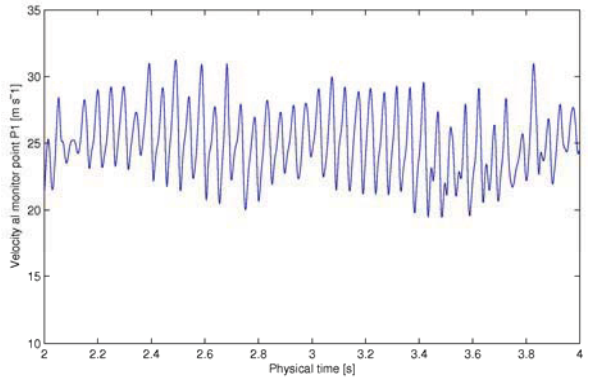

Figure 2.18: Absolute value of the time-dependent velocity at monitor point P1, Config. 3

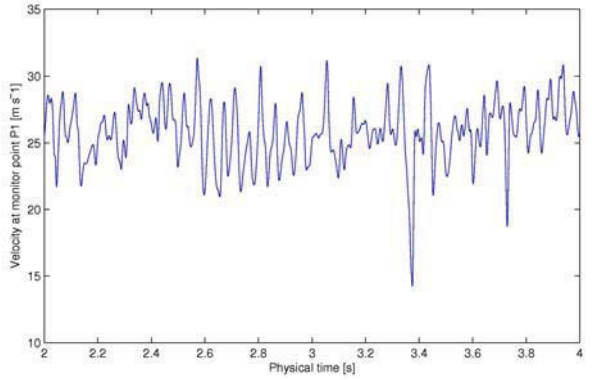

Figure 2.19: Absolute value of the time-dependent velocity at monitor point P1, Config. 4

Remarks and conclusions

The RST-simulations discussed in this paper require thorough pre-convergence with spatial discretization schemes of lower order (such as UDS1) in order to arrive at numerically stable simulations when using a higher order scheme.

There is an axially stretched recirculation zone located at the lower part of the main cylinder, cf. Figure 2.16. Recirculation zones of this kind have also been observed in [3] for some configurations studied there. In the terminology used in [3] the points with high axial vorticity are connected to the phenomenon of (precessing) vortex breakdown. In Figure 2.17 an isosurface plot of the time-averaged *z*-vorticity is shown for $\langle\omega_z\rangle = 250\ s^{-1}$.

In contrast to [3], where the RST-simulations show temporal periodicity of the time-dependent velocity field at the monitor points, the temporal behavior of the velocity field observed in the current RST-simulations is more irregular. However, the computations with the coarser mesh and the larger time step (Config. 3) show a more regular behavior than the computations with the finer mesh and the smaller time step (Config. 4), see Figures 2.18 and 2.19. (The coordinates of the monitor point P1 in Figures 2.18 and 2.19 are P1 = (-0.26 m; 0.05 m; 0.26 m).) One could therefore speculate that at least one reason for this discrepancy between [3] and the current results is that in [3] a coarser grid was used to perform the simulations. It is likely that a second reason for the discrepancy is that a different geometric configuration was studied in [3]: In [3] more inlet and outlet pipes are considered, and the injection angles of the pack- and recirc-airstreams differ from 90°. A further reason might be that the Reynolds numbers of the configurations studied in [3] are smaller than the Reynolds number of the current configuration. More precisely, the ratio of the Reynolds numbers (based on the diameter of the central cylinder and the mean velocity in the central cylinder) of the current configuration and the configuration described in [3] is approximately $Re_{current} / Re_{Bourlart\ et\ al.} = 2.2$.

The simulations in the highly symmetric geometry show that the time-averaged flow field has (at least) two different realizations which are related to one another by a symmetry transformation. Since the symmetry of the flow field is lower than the symmetry of the geometry, the boundary data and the initial data, the parity of the flow field must be determined “by chance” in the current simulations. In fact, it was possible to obtain a solution with the opposite direction of rotation of the large vortex in the main cylinder by starting the computation with suitably modified initial conditions. Ongoing experiments that are performed at FH JOANNEUM indicate that in a real mixing unit – when temporal fluctuations of the inflow parameters are present – the flow field orientation changes parity in a chaotic and non-predictable manner. However, in the simulations described in this article no change of the direction of rotation of the core vortex is observed. It is therefore conceivable that – under strictly symmetric and steady inflow conditions – the flow field, once it has adjusted to a certain direction of rotation, is indeed stable with respect to *infinitesimal* perturbances, but the perturbances in the experiments have been too large to produce a stable vortex. Another explanation for the discrepancy between the simulation results and the experimental observations could be that the flow field orientation is always unstable (no matter how small the fluctuations of the inflow parameters are), but this cannot be seen in the actual simulations because not enough physical time was simulated in order to observe flipping of the core vortex.

The current simulations show, when compared with each other, good agreement for the target variables “pressure loss”, “mass flow rate” and “mass fraction”. This is remarkable, since predictions of scale-resolving and non-scale-resolving turbulence models of thermal and scalar mixing may differ significantly for certain configurations. For instance, a well-documented test case where classical RANS-models such as the k–ε model dramatically fail to predict the experimental results is thermal mixing in an ordinary T-junction [6, 12]. A reason for the good agreement of the current SAS-SST and RST simulations with respect to scalar mixing might be that the turbulence production in the region of the colliding jets is very strong. Therefore the RST model might resolve the turbulent eddies in this region sufficiently well in order to predict a similar scalar mixing as the SAS model.

As can be seen from Table 2.8 the “mixing performance” of this simple symmetric manifold – measured by the mass fractions M_1 and M_2 – is predicted by the current simulations to be almost 90%.

The current simulations do not allow a clear decision which of the two turbulence models – the SAS-SST model on the one hand and the RST-model on the other hand – describe the physics in the symmetric MU more realistically. However, from a purely computational point of view the SAS-model must be preferred since it requires the solution of only two additional equations, whereas the RST-model requires the integration of seven additional partial differential equations. Furthermore, the SAS-model is more robust, and pre-convergence with a scheme of lower order is unnecessary, cf. Table 2.3. Therefore, and since SAS-SST predicts thermal mixing in T-pipes reasonably well, the authors will preferably utilize the SAS-model (accompanied with LES simulations) for further investigations of the flow-physics in mixing manifolds.

Acknowledgements

The authors are very grateful to the referee. His or her comments and remarks helped to improve the quality of the paper substantially.

REFERENCES

[1] ANSYS-CFX (2007), Version 11.0, Copyright 1996-2007 ANSYS Europe LTd.

[2] T.J. Barth and D.C. Jesperson, *The Design and Application of Upwind Schemes on Unstructured Meshes,* AIAA-Paper 89-0366, 1989.

[3] R. Bourlart and F. Landais, *Effect of Swirl Flows in Aeronautical Mix Manifolds,* Journal of Aircraft **44** (2), 2007, 476-486.

[4] J. Eggebrecht, H. Rogers, A. Yorozu and Boeing, *Air Conditioning System and Air Mixing/Water Separation Apparatus Therein,* U.S. Patent 4517813, field 21 May 1985.

[5] J.H. Ferziger and M. Peric, *Computational Methods for Fluid Dynamics,* Springer, 3rd ed., 2002.

[6] T. Frank, C. Lifante, M. Adlakha, H.M. Prasser and F. Menter, *Simulation of Turbulent and Thermal Mixing in T-Junctions using URANS and Scale-Resolving Turbulence Models in ANSYS CFX,* Experiments and CFD Code Applications to Nuclear Reactor Safety OECD/NEA CEA Workshop, Grenoble, France, 10-12 September 2008.

[7] F.R. Menter, *Two-Equation Eddy-Viscosity Turbulence Models for Engineering Applications,* AIAA Journal **32**, 1598-1605, 1994.

[8] F.R. Menter, *Eddy-viscosity Transport Equations and their Relation to the $k-\varepsilon$ Model,* Trans. ASME, J. Fluids Eng. **119**, 876-884, 1997.

[9] F.R. Menter, Y. Egorov, *A Scale-Adaptive Simulation Model using Two-Equation Models,* 43rd AIAA Aerospace Sciences Meeting and Exhibit, 10-13 January 2005, Reno, Nevada.

[10] Menter and Y. Egorov, *Revisiting the turbulent scale equation,* in IUTAM Symposium on One Hundred Years of Boundary Layer Research Proceedings of the IUTAM Symposium held at DLR-Göttingen, Germany, August 12-14, 2004.

[11] J.C. Rotta, *Turbulente Strömungen*, Teubner Verlag, Stuttgart, 1972.

[12] J. Westin, F. Alavyoon, L. Andersson, P. Veber, M. Henriksson and C. Andersson, *Experiments and Unsteady CFD-Calculations of Thermal Mixing in a T-Junction*, OECD/NEA/IAEA Workshop on the Benchmarking of CFD Codes for Application to Nuclear Reactor Safety (CFD4NRS), Munich, Germany, 1-15, 2006.